Wall slip of bubbles in foams

A. Saugey, W. Drenckhan, and D. Weaire
School of Physics, Trinity College, Dublin 2, Ireland

(Received 9 December 2005; accepted 24 March 2006; published online 5 May 2006)

We present a computational analysis of the flow of liquid foam along a smooth wall, as encountered in the transport of foams in vessels and pipes. We concentrate on the slip of the bubbles at the wall and present some novel finite element calculations of this motion for the case of fully mobile gas/liquid interfaces. Our two-dimensional simulations provide for the first time the bubble shapes and entire flow field, giving detailed insight into the distribution of stresses and dissipation in the system. In particular, we investigate the relationship between the drag force and the slip velocity of the bubble, which for small slip velocities obeys power laws, as predicted by previous semianalytical treatments. © *2006 American Institute of Physics*. [DOI: 10.1063/1.2196912]

I. INTRODUCTION

Many important processes in industrial chemistry[1,2] and recent developments in microfluidics[3] involve the motion of liquid foams in vessels and pipes. Such foams consist of discrete gas bubbles immersed in a continuous liquid phase,[2] stabilized by surface active agents (surfactants). As a result, they are anything but simple fluids, even though their individual components might be.[4]

The analysis of the flow of such materials presents a complex problem to experiment, theory, and computer simulation. Here we shall concentrate on one key aspect, namely *wall slip*, which refers to the sliding motion of the foam bubbles along a smooth wall. We will present some novel simulations of this motion.

Two related experimental scenarios are illustrated in Fig. 1. In the first case, foam is contained between the plates of a classical rheometer with a smooth wall.[5,6] In the second, ordered foam structures[7,8] are driven through a narrow channel by a pressure gradient.[9] In both cases, the sliding motion of the foam along the wall is opposed by a dissipative force F_D, which is attributed to the viscous behavior of the liquid phase at the wall. Roughly speaking, the bubbles "aquaplane" on a thick liquid film, the so-called wetting film. F_D increases with the slip velocity U_0, but the relationship between F_D and U_0 is not the familiar one of simple proportionality, even if the liquid may be assumed to be Newtonian. The complication resides within the geometry, which changes with the velocity and entails nontrivial scaling laws.

Previous theoretical treatments used a lubrication approximation to describe the liquid flow near the wall as a unidirectional flow, which reduces the calculation of the bubble shape to the solution of a one-dimensional problem. These concepts were introduced by Bretherton[10] for the sliding motion of individual bubbles, and were extended to foams and emulsions by Kraynik[11] and Princen.[12] Recently they have been re-invoked and elaborated for foams by Terriac *et al.*[13] and Denkov *et al.*[6]

These authors derived power laws for the force-velocity relation:

$$F_D = \lambda U_0^n, \tag{1}$$

with $n=2/3$ (commonly called the Bretherton law[10]) in the case of *tangentially mobile* gas/liquid interfaces (zero interface viscosity or zero tangential stress), and $n=1/2$ when the interface is assumed *tangentially immobile* (infinite interface viscosity or zero interface velocity). The prefactor λ may be called the "viscous drag coefficient."[9,14] Its value depends on the interfacial mobility and the ratio of liquid volume to gas volume of the system. These power laws were found to hold for small slip velocities and are in reasonable agreement with appropriate experiments.[3,6,9]

Extending current theories to larger slip velocities proves difficult. Also, neither of the proposed models can provide the precise shape of the entire gas/liquid interface. We have therefore undertaken a computational approach, using a finite element technique, to find the flow pattern of an incompressible fluid coupled with a moving boundary under surface tension. A detailed description of the model is given in Sec. II.

Using FEMLAB software (version 3.1), we can compute the complete velocity field and interface geometry consistent with the stress on the interfaces that is associated with the flow. This is, to our knowledge, the first full-scale simulation of this kind to be accomplished and offers the prospect of a reexamination and extension of previous approximative theories.

In this article, we shall consider in detail only the ideal of a tangentially mobile interface. Some comments on fully and partially immobile interfaces are given at the end in Sec. V.

Finite element techniques have already been employed to study the drainage in liquid foams,[15–17] particularly the influence of the interfacial shear viscosity on the liquid flow between bubbles assuming fixed geometries. In our case, the geometry must be computed together with the flow, as they are highly interdependent. A specific formulation of the appropriate equations is employed, as described in Sec. III.

The results of our simulation, presented in Sec. IV, are in excellent agreement with the conclusions of Bretherton[10] within the appropriate velocity regime, for which his scaling

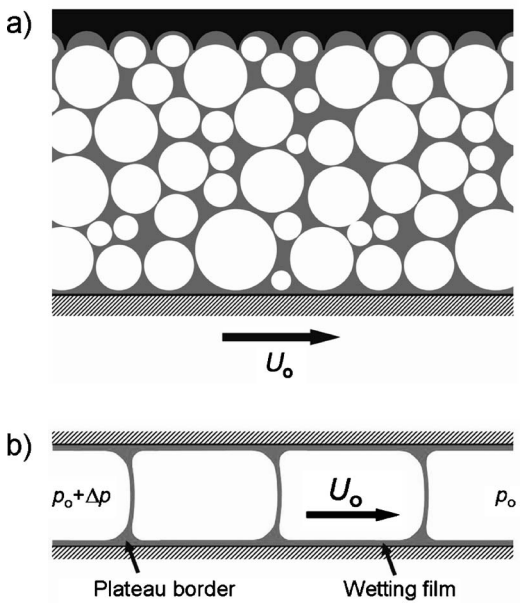

FIG. 1. Sketch of two typical experiments to study wall slip of a liquid foam. (a) Foam is sheared in a rheometer between a smooth and a rough plate moving at relative velocity U_0. (b) A train of equal volume bubbles is pushed through a narrow channel at velocity U_0 by a pressure drop Δp.

law holds. We extend the present calculations to significantly higher slip velocities. We are also able to expose many relevant details not previously accessible, since the entire flow and shape patterns are determined. In particular, the precise distribution of dissipation can be identified.

II. DEFINITION OF THE MODEL

In keeping with previous work, the model system is two-dimensional, as illustrated in Fig. 2. A bubble is pressed against a flat wall, with periodic boundary conditions on either side. This represents in effect the near-wall region of an infinite train of identical bubbles sliding on a liquid film (the "wetting film"). The bubbles are separated by thin films which are connected to the wetting film by so-called Plateau borders[2] [see Fig. 1(b)].

It is convenient to adopt the frame of reference in which the bubbles are stationary and the wall moves with velocity U_0 [Fig. 2(a)], and we shall do so throughout this article. The liquid in the wetting film and in the surface Plateau borders is dragged along by the wall motion.

The gas/liquid interface is required to be in equilibrium under the various forces acting on it [sketched in Fig. 2(b)]. The stress $\underline{\underline{\sigma}}$ in the liquid consists of an isotropic pressure p_L together with the deviatoric (or shear) stress. This exerts a normal force on the gas/liquid interface, which is subject to a surface tension γ. There are also short-range repulsive interactions between the interfaces, and between interface and wall, commonly called the disjoining pressure Π.

No stress (e.g., viscous or Marangoni[18,19]) acts *within* the surface in the present model.

The following subsections describe the bulk equations and the corresponding boundary conditions, which are solved numerically. Two key nondimensional parameters are

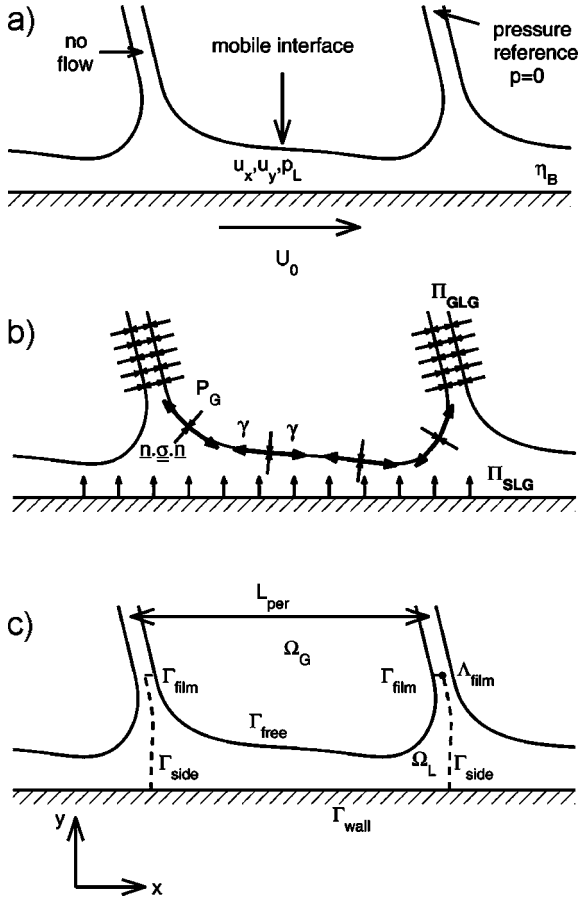

FIG. 2. Sketch of a sliding bubble. (a) Gas bubbles are immersed in a liquid of viscosity η_B, flow field $u(x,y)$, and pressure field $p_L(x,y)$. They slide along a smooth wall at velocity U_0 and are separated from the wall and from each other by thin liquid films. In the latter we set a pressure reference, equivalent to a reservoir at constant pressure. The gas/liquid interface is assumed to be fully mobile. The bubbles are stationary while the wall moves at U_0. (b) The stress balance on the gas/liquid interface takes into account the normal stress $\underline{n}\cdot\underline{\underline{\sigma}}\cdot\underline{n}$ exerted by the liquid, the surface tension γ, the disjoining pressures Π in the thin films and the gas pressure P_G. (c) Definition of the unit cell of length L_{per} with periodic boundary conditions on either side Γ_{side}. The gas/liquid interface Γ_{free} separates the gas domain Ω_G and liquid domain Ω_L. On the liquid film boundary Γ_{film} we apply a special point boundary condition (pressure reference) at Λ_{film} [see (a)].

extracted from this formulation, namely the capillary number Ca, which is proportional to the wall velocity U_0, and the scaled length L_{per} of the periodic cell, representing the length of the bubble (see Fig. 2).

A. Bulk equations

The pressure P_G in the gas domain Ω_G is the same everywhere ($p_G=P_G$). Since only relative pressures have any significance here, its value is arbitrary and can be set equal to zero for our purposes:

$$P_G = 0. \tag{2}$$

With such an offset, the calculated values of the liquid pressures will be negative in some regions.

The pressure p_L in the liquid domain Ω_L may be considered to be the sum of a static pressure P_L which obtains

whenever the system is static, and a dynamic pressure $p(x,y)$ which is due to the flow and varies with position.

For low Reynolds numbers and steady incompressible liquid flow in the domain Ω_L (see Fig. 2), the velocity field

$$\underline{u} = \begin{pmatrix} u_x \\ u_y \end{pmatrix} \tag{3}$$

is described by the Stokes equations:

$$\nabla \cdot \underline{\underline{\sigma}} = 0, \tag{4}$$

$$\nabla \cdot \underline{u} = 0. \tag{5}$$

Here $\underline{\underline{\sigma}}$ is the stress tensor for a Newtonian liquid, related to the velocity field by

$$\underline{\underline{\sigma}} = -p_L \underline{\underline{1}} + \eta_B[\nabla \underline{u} + (\nabla \underline{u})^T], \tag{6}$$

where η_B is the bulk viscosity. The deformation rate tensor $\underline{\underline{\epsilon}}$ is given by

$$\underline{\underline{\epsilon}} = \frac{1}{2}[\nabla \underline{u} + (\nabla \underline{u})^T]. \tag{7}$$

Gravity is neglected, as the typical size of a Plateau border is smaller than 10^{-3} m, which leads to very small Bond numbers (ratio of gravitational to surface tension forces).

B. Boundary equations

We adopt a set of boundary conditions which are physically consistent but do not attempt to fully represent any particular experiment. In general terms:

- The system has translational symmetry, i.e., the pressures on either side of the bubble are equal.
- The thin liquid films separating the bubbles are assumed to be in equilibrium with a large reservoir at constant pressure, i.e., the liquid volume is not fixed.

Various notations and features of the boundary conditions are depicted in Fig. 2.

1. Liquid/wall interface Γ_{wall}

The wall is moving with a velocity U_0 in the x direction [Fig. 2(a)]. We assume that there is no slip between the wall and the liquid, therefore

$$\underline{u} = \begin{pmatrix} U_0 \\ 0 \end{pmatrix}. \tag{8}$$

2. Liquid/liquid side boundaries Γ_{side}

We apply periodic boundary conditions on $\underline{u}$ and p_L on the left- and right-hand side. The same periodicity is in effect imposed on P_G, as it is the same in each bubble.

3. Film Γ_{film}

We assume the liquid to be at rest in the thin film that separates the bubbles:

$$\underline{u} = \begin{pmatrix} 0 \\ 0 \end{pmatrix}. \tag{9}$$

At a reference point Λ_{film} [Fig. 2(a)] we set

$$p_L = P_L, \tag{10}$$

which implies zero dynamic pressure, since $p = p_L - P_L = 0$ (see Sec. II A). This is equivalent to saying that the film is in equilibrium with a liquid reservoir at static pressure P_L. It also implies that the amount of liquid in the system adjusts to maintain this pressure condition. This is justified in the rheometer experiments shown in Fig. 1(a), in which the reservoir is provided by the surrounding foam. For the case of foam flow in narrow tubes it seems more appropriate to apply a constant volume constraint. This can be implemented in FEMLAB, but is not considered further in this article.

4. Gas/liquid interface Γ_{free}

We consider the case of a tangentially mobile gas/liquid interface, which corresponds to zero interface viscosity or zero tangential stress exerted by the boundary. Therefore,

$$\begin{aligned} &\underline{u} \cdot \underline{n} = 0, \\ &\underline{n} \cdot \underline{\underline{\sigma}} \cdot \underline{t} = 0, \end{aligned} \tag{11}$$

with $\underline{n}$ and $\underline{t}$ being the interface normal and tangent, respectively.

The equilibrium of the normal forces on an element of free interface of surface tension γ and radius of curvature r requires the local force balance

$$P_G - \gamma r^{-1} - \Pi + \underline{n} \cdot \underline{\underline{\sigma}} \cdot \underline{n} = 0. \tag{12}$$

r is defined to be positive along the outward normal of the liquid domain. Π represents the disjoining pressure,[20] which provides a short-range, repulsive force between the interfaces. The equilibrium condition (12) is essentially that expressed by the familiar Young-Laplace law.[21]

In foams the disjoining pressure is a result of the interaction of surfactants adsorbed at the interface. A commonly used expression for Π is

$$\Pi(d) = \frac{C}{d^m}, \tag{13}$$

where d is the separation between the interfaces and C and m depend on the surfactant and the type of interfaces (gas/liquid or liquid/wall). In what follows, Π is significant only in the films of which there are two kinds, namely the thin film between the bubbles and the wetting film, with disjoining pressures Π_{GLG} and Π_{SLG}, respectively. Π is therefore implemented as

$$\Pi = \Pi_{GLG} + \Pi_{SLG} = \frac{C_{GLG}}{d_{GLG}^m} + \frac{C_{SLG}}{d_{SLG}^m}, \tag{14}$$

with $m=8$.

In real foams, film thicknesses are of order 10^{-7} m, which is very much smaller than the capillary radius $R = \mathcal{O}(10^{-4}$ m) of the Plateau border. Finite element techniques are not capable of resolving such difference in length

scales. We therefore implement a nonphysical disjoining pressure. This is justified, as we are only interested in the flow regime with thick wetting films, in which the disjoining pressure is negligible. The inclusion of this artificial disjoining pressure nevertheless provides some qualitative insight into its role. For a more detailed discussion see Sec. III D.

C. Scaling

We introduce the following constants for scaling purposes:

$$\text{velocity scale} \quad U = \gamma \eta_B^{-1}, \tag{15}$$

$$\text{pressure scale} \quad P = P_G - P_L, \tag{16}$$

$$\text{length scale} \quad R = \gamma P^{-1} \text{ (capillary radius)}. \tag{17}$$

The reduced variables are therefore

$$\hat{x} = R^{-1}\, x, \tag{18}$$

$$\hat{y} = R^{-1}\, y, \tag{19}$$

$$\hat{L}_{\text{per}} = R^{-1}\, L_{\text{per}}, \tag{20}$$

$$\hat{\underline{u}} = U^{-1}\, \underline{u}, \tag{21}$$

$$\hat{p} = P^{-1}\, p, \tag{22}$$

$$\hat{\nabla} = R\ \nabla, \tag{23}$$

$$\hat{\Delta} = R^2\, \Delta. \tag{24}$$

As is conventional we introduce the capillary number Ca

$$Ca = \frac{\eta_B U_0}{\gamma}. \tag{25}$$

Equations (4), (5), (8), (9), and (12) are then simplified to

$$\hat{\Delta}\hat{\underline{u}} = \hat{\nabla}\hat{p} \quad \text{on } \Omega_L, \tag{26}$$

$$\hat{\nabla} \cdot \hat{\underline{u}} = 0 \quad \text{on } \Omega_L, \tag{27}$$

$$\hat{\underline{u}} = \begin{pmatrix} Ca \\ 0 \end{pmatrix} \quad \text{on } \Gamma_{\text{wall}}, \tag{28}$$

$$\hat{\underline{u}} = \begin{pmatrix} 0 \\ 0 \end{pmatrix} \quad \text{on } \Gamma_{\text{film}}, \tag{29}$$

$$\underline{n} \cdot \hat{\underline{\underline{\sigma}}} \cdot \underline{n} - \hat{\Pi} = \hat{\nabla}_S \cdot \underline{n} \quad \text{on } \Gamma_{\text{free}}, \tag{30}$$

where $\hat{\nabla}_S = (\underline{\underline{I}} - \underline{n}\,\underline{n})\hat{\nabla}$ denotes the surface gradient operator, with the surface identity tensor $(\underline{\underline{I}} - \underline{n}\,\underline{n})$.[22] The rescaling exposes the role of the two key parameters Ca and $\hat{L}_{\text{per}}$. Ca represents the wall velocity if γ and η_B are considered fixed, and $\hat{L}_{\text{per}}$ the size of the bubbles through the definition of Ω_L.

The reduced viscous force on the wall $\hat{F}_D = \gamma^{-1} F_D$ is given by

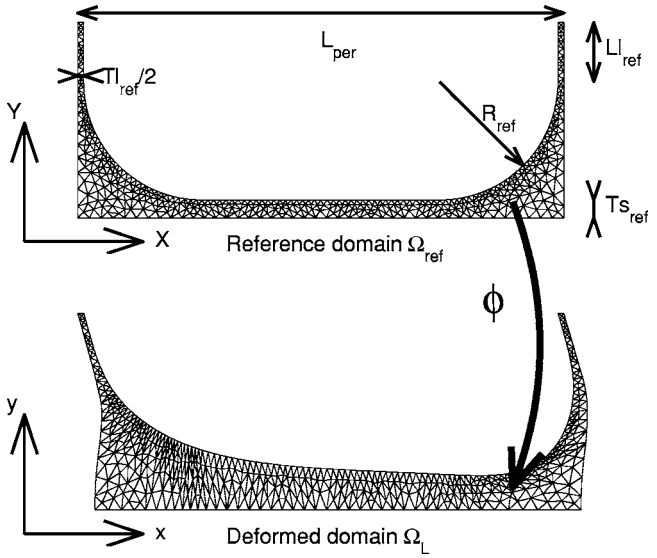

FIG. 3. A transformation ϕ is computed, which maps the reference domain Ω_{ref} onto the deformed physical domain Ω_L. The flow equations are then mapped onto Ω_{ref} using ϕ^{-1} and solved there.

$$\hat{F}_D = \int_{\text{wall}} \underline{t} \cdot \hat{\underline{\underline{\sigma}}} \cdot \underline{n}\, d\hat{x}. \tag{31}$$

Note, for clarity, the symbol ^ will be removed from now on. Only reduced variables are used.

III. COMPUTATIONAL BACKGROUND

Various methods of addressing the problem of incompressible fluid flow with moving boundaries have been reported in the literature.[23–27] Most of them employ a time dependent Arbitrary Lagrangian-Eulerian (ALE) formulation of the problem. Its principle resides in defining a fixed reference domain Ω_{ref} which is mapped onto the physical domain Ω_L by a generally time dependent transformation ϕ which satisfies appropriate displacement conditions. Using the inverse of this transformation, the Navier-Stokes equations are projected onto the reference domain Ω_{ref}. A finite element technique is then applied on Ω_{ref} to define a mesh and to solve the projected equations.[28] Doing so corresponds to solving the original equations on the mesh mapped by ϕ onto the deformed domain.

We implement a modified version of this procedure in FEMLAB to focus on stationary regimes. The following sections present a brief overview of the formulation to point out its physical relevance to our problem. For a detailed description we refer the reader to Refs. 23, 24, 26, and 28 and to the FEMLAB documentation (version 3.1).

A. Reference domain and deformed domain

Key ingredient of any ALE formulation is the definition of the transformation ϕ of the reference domain Ω_{ref} onto the physical domain Ω_L. For our computations, we chose Ω_{ref} such that it is similar to that of the static solution of the problem (Fig. 3). Ω_{ref} is described by (X, Y) coordinates. It consists of two half Plateau borders with radius of curvature

R_{ref} with half a liquid film of thickness $Tl_{\text{ref}}/2$ and length Ll_{ref} above. The Plateau borders are linked by a wetting film of thickness Ts_{ref} such that the total width of Ω_{ref} matches the given length of the periodic cell L_{per}. R_{ref}, Tl_{ref}, and Ts_{ref} are defined such that Ω_{ref} is as close as possible to the expected deformed domain Ω_L. Ll_{ref} is kept small to reduce computation times but large enough to obtain a finite liquid film at the end of the simulations.

The transformation ϕ maps (X,Y) in Ω_{ref} onto (x,y) in Ω_L

$$(x,y) = \phi(X,Y), \tag{32}$$

such that it satisfies the following physical boundary conditions:

- the boundary Γ_{film} is assumed fixed, i.e., $x=X$ and $y=Y$ on Γ_{film},
- (x,y) satisfies the normal force equilibrium on the free interface (30).

Additional computational conditions are needed to ensure that a good quality mesh is obtained after the transformation. We therefore choose

- a symmetry condition on Γ_{wall}: $\partial x/\partial Y=0$,
- translational periodic conditions on Γ_{side}: $(x_{\text{left}}=x_{\text{right}}-L_{\text{per}}\ y_{\text{left}}=y_{\text{right}})$.

On Γ_{free}, the normal force equilibrium (30) does not impose a condition on the tangential displacement of a node along the free interface. We therefore introduce the relationship

$$(x-X)n_Y - (y-Y)n_X = 0. \tag{33}$$

This ensures that a point on the interface is displaced along the normal of Ω_{ref}. After implementing these boundary conditions, the motion of a point in the interior of the domain is defined by the partial differential equation

$$\Delta\phi = 0. \tag{34}$$

Although some recent work[24] reports improved results with more complex descriptions of ϕ, the one presented here proved sufficient for our problem.

B. Weak formulation of the force balance on the interface

The various conditions given in Sec. III A define a closed set of equations which can be solved by a finite element procedure. For this, a "weak formulation" of Eq. (30) is needed. This well known feature of finite element techniques gives less restriction on the solution and more precise results.[28] The weak formulation of Eq. (30) has been derived by Cairncross[24] for the three-dimensional case.

For a one-dimensional free interface given by its coordinates $(\alpha(s),\beta(s))$ in any local frame (e_α,e_β), the appropriate form is

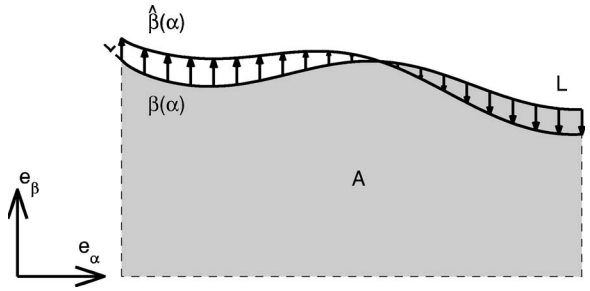

FIG. 4. The weak form can be viewed as the virtual work associated with an infinitely small displacement of an interface of length L associated with a liquid domain of area A.

$$\begin{aligned} 0 = &-(P_G + \underline{n}\cdot\underline{\underline{\sigma}}\cdot\underline{n})\int \tilde{\beta}\frac{\partial\alpha}{\partial s}ds + \gamma\int \frac{\partial\beta}{\partial s}\frac{\partial\tilde{\beta}}{\partial s}\left\{\left(\frac{\partial\alpha}{\partial s}\right)^2 \right. \\ &\left. + \left(\frac{\partial\beta}{\partial s}\right)^2\right\}^{-1/2} ds + \gamma\left[\tilde{\beta}\frac{\partial\beta}{\partial s}\left\{\left(\frac{\partial\alpha}{\partial s}\right)^2 \right.\right. \\ &\left.\left. + \left(\frac{\partial\beta}{\partial s}\right)^2\right\}^{-1/2}\right]_{s=0}^{s=1} \end{aligned} \tag{35}$$

for any virtual displacement $\tilde{\beta}$ (Fig. 4). Defining the area A and the length L of the interface as

$$A = \int \beta\frac{\partial\alpha}{\partial s}\,ds, \quad L = \int \left\{\left(\frac{\partial\alpha}{\partial s}\right)^2 + \left(\frac{\partial\beta}{\partial s}\right)^2\right\}^{1/2} ds, \tag{36}$$

the first term on the right-hand side of Eq. (35) can be interpreted as a volume term and the second and third as a surface term for the virtual work.

Equation (35) is only valid for any frame (e_α,e_β) as long as $\partial\alpha/\partial s \neq 0$. As this is not the case for our geometry, we describe the free interface in the left and right half of our periodic cell in two different frames, namely

$$e_\alpha = \frac{1}{\sqrt{2}}(e_X - e_Y), \quad e_\beta = \frac{1}{\sqrt{2}}(e_X + e_Y) \quad \text{for the left half,} \tag{37}$$

$$e_\alpha = \frac{1}{\sqrt{2}}(e_X + e_Y), \quad e_\beta = \frac{1}{\sqrt{2}}(e_X - e_Y) \quad \text{for the right half.} \tag{38}$$

We implement the reduced form of expression (35) in FEMLAB.

The derivations of this section emphasize that the shape (x,y) [or equivalently (α,β) in Eq. (35)] of the physical domain Ω_L is given by a nonlinear system of equations. It is strongly coupled with the flow field through the normal stress term $\underline{n}\cdot\underline{\underline{\sigma}}\cdot\underline{n}$.

C. Projection of the fluid equations on the reference domain

Equations in Secs. III A and III B govern the deformation of the reference domain and its associated mesh to fit the physical domain Ω_L. Instead of solving the Stokes equations

(26) and (27) on the deformed mesh, they are projected on the reference mesh via the inverse of ϕ once written in the weak form.

The weak formulation of Stokes equations is derived from the virtual power principle. This states that the velocity field $\underline{u}$, the pressure field p_L, and their associated stress tensor $\underline{\underline{\sigma}}$ satisfies[29]

$$\int_{\Omega} \underline{\underline{\sigma}}:\nabla\underline{\tilde{v}} + \nabla\underline{u}:\tilde{p}\underline{\underline{1}}\, d\Omega = 0, \tag{39}$$

for any virtual velocity field $\underline{\tilde{v}}$ which is in accordance with the kinematic flow conditions and virtual pressure field $\tilde{p}$.

We project Eq. (39) onto Ω_{ref} by rewriting $\nabla\underline{u}$ in terms of the gradient ∇_{ref} in (X,Y) coordinates and the inverse Jacobian $\underline{\underline{J}}^{-1}$ of ϕ:

$$\nabla\underline{u} = \nabla_{ref}\underline{u} \cdot \underline{\underline{J}}^{-1}, \tag{40}$$

$$\underline{\underline{J}}^{-1} = \frac{1}{D}\begin{bmatrix} \dfrac{\partial y}{\partial Y} & -\dfrac{\partial x}{\partial Y} \\ -\dfrac{\partial y}{\partial X} & \dfrac{\partial x}{\partial X} \end{bmatrix}, \tag{41}$$

$$D = \frac{\partial x}{\partial X}\frac{\partial y}{\partial Y} - \frac{\partial x}{\partial Y}\frac{\partial y}{\partial X}. \tag{42}$$

Equation (39) then becomes

$$\int_{\Omega_{\mathrm{ref}}} [-p_L\underline{\underline{1}} + \eta_B(\nabla_{\mathrm{ref}}\underline{u} \cdot \underline{\underline{J}}^{-1} + {}^t(\nabla_{\mathrm{ref}}\underline{u} \cdot \underline{\underline{J}}^{-1}))]:[\nabla_{\mathrm{ref}}\underline{\tilde{v}} \cdot \underline{\underline{J}}^{-1}] + \tilde{p}\underline{\underline{1}}:[\nabla_{\mathrm{ref}}\underline{u} \cdot \underline{\underline{J}}^{-1}]D d\Omega_{\mathrm{ref}} = 0. \tag{43}$$

This expression is linear in terms of the flow variables u_x, u_y, and p_L and depends on the shape variables (x,y) by the inverse Jacobian $\underline{\underline{J}}^{-1}$.

D. Simulation

Equations (28), (29), (35), and (43) define the set of coupled, stationary, nonlinear partial differential equations for our problem, which we solve in FEMLAB. Both surface shape and liquid flow variables are included in a single set of equations to be directly solved using the built-in nonlinear Newton algorithm.

We start the computations with a small value of *Ca* for which we know that the domain deforms very little. As an initial guess for the Newton algorithm we use the reference geometry Ω_{ref} $(x=X, y=Y)$, $u_x=0, u_y=0$ and $p=P_L$. Having obtained the converged solution, we iteratively increase *Ca* with logarithmic step size. At each step we use the previous solution as an initial guess while keeping the reference geometry unchanged. A number of converged solutions for increasing *Ca* are displayed in Fig. 5 (solid line) together with the reference domain (dashed line).

As *Ca* is varied, we find three distinct regimes, which are described in the following. Understanding their key features allows us to choose physically relevant and correct ingredients and parameter ranges for further simulations and analysis. To demonstrate the distinction between the regimes, the force F_D on the wall is plotted in Fig. 6(a). Also shown in Fig. 6(b) is the quantity

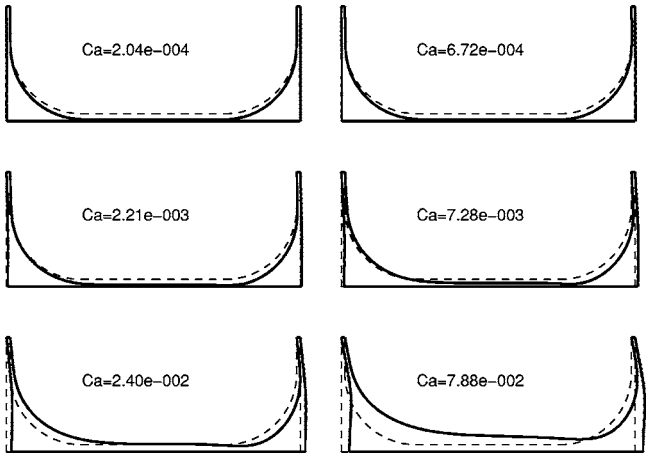

FIG. 5. Variation of the bubble shape (solid line) with the capillary number *Ca*. The dashed line represents the reference domain Ω_{ref}.

$$n = \frac{\partial \log(F_D)}{\partial \log(Ca)}, \tag{44}$$

which presents the index of the power law relationship in Eq. (1) whenever it is reasonably constant. The six surfaces displayed in Fig. 5 correspond to the + symbols in Fig. 6(a).

(1) *Quasistatic regime* (images 1–3 in Fig. 5): For small *Ca* the shape of the bubble is approximately that of the static case, being fully determined by the disjoining pressure Π and the capillary radius $R=P_G-P_L$. F_D varies linearly with *Ca* (dotted line in Fig. 6).

(2) *Scaling regime* (images 4–6 in Fig. 5): As *Ca* increases, the normal stresses on the free interface increase, which has two effects. In the wetting film they eventually overcome the static value of the disjoining pressure Π_{SLG} [compare Eqs. (30) and (14)] and the film thickens, with Π_{SLG} becoming negligible. Results for F_D are given by the solid line in Fig. 6. The high power $m=8$ chosen for the disjoining pressure in Eq. (14) ensures a sharp transition between the quasistatic regime and the scaling regime, whose transition point we define where $\Pi_{SLG}/(P_G-P_L)<5\%$. Second there is a progressive deformation of the rest of the free interface.

(3) *Thick film regime*: At even higher capillary number, the thickness h_{film} of the wetting film becomes of the same order as the capillary radius *R*. This regime is beyond the scope of current experiments, nor can it be compared with previous theoretical results. We identify this regime with $h_{\mathrm{film}}/R>20\%$ (dashed line in Fig. 6).

In the remainder of the article we focus on the *scaling regime* of intermediate *Ca* $(10^{-6}<Ca<10^{-1})$, which covers most foam rheology experiments.[3,4,6,9,13] In this range, the wetting film is sufficiently thick such that the disjoining pressure can be neglected.[6] However, computing the flow over the whole range of *Ca* causes convergence issues due to large mesh deformations (e.g., the wetting film thickness

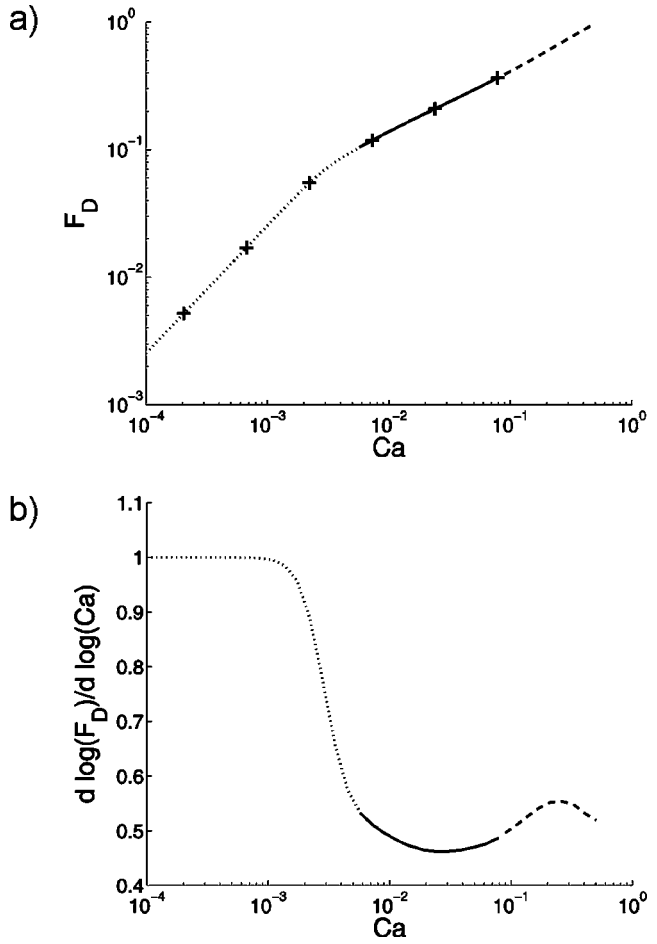

FIG. 6. (a) Reduced friction force [Eq. (31)] exerted by the bubble on the wall as a function of its velocity, given by *Ca*. The + symbols correspond to the six cases shown in Fig. 5. The line styles represent three distinct regimes: disjoining pressure (dotted line), interest in this article (full line), and thick film (dashed line). (b) Slope of (a) in a log-log plot, which represents n in Eq. (1) whenever it is reasonably constant.

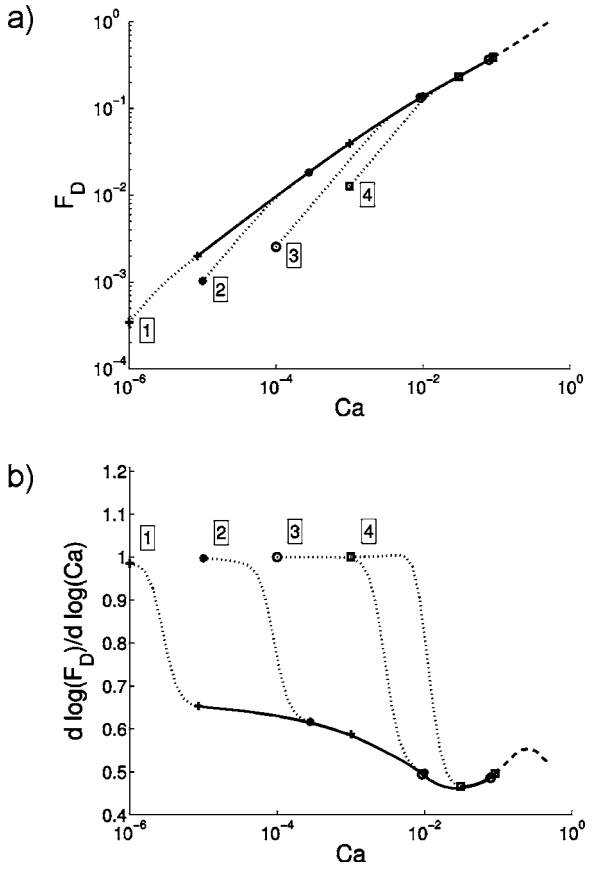

FIG. 7. Same graphs as in Fig. 6, but here we show four computational cycles run for different ranges of *Ca* with appropriately adjusted disjoining pressures. 1: $C_{SLG}=(2\times10^{-4})^m$, 2: $C_{SLG}=(2\times10^{-3})^m$, 3: $C_{SLG}=(2\times10^{-2})^m$, and 4: $C_{SLG}=(5\times10^{-2})^m$ in Eq. (14). The symbols mark the beginning and the end of the scaling regime (solid line) of each cycle according to the definitions given in the text. All solutions in this regime collapse on a single curve.

goes from 0.001 to 0.2). We therefore run several cycles of computations for smaller ranges of *Ca* (Fig. 7). For each cycle, the reference mesh is defined such that we ensure small mesh deformations over the chosen range of *Ca*. To stabilize the computations in the quasistatic regime at the beginning of each cycle, we artificially adjust the magnitude of the disjoining pressure such that for the smallest value of *Ca* the dynamic stresses in the wetting film are negligible. Typical orders of magnitude of the implemented reduced disjoining pressure $\Pi=\Pi_{SLG}+\Pi_{GLG}$ in Eq. (14) are $C_{SLG}=0.01^m$, $C_{GLG}=0.1^m$, with $m=8$ (see also caption of Fig. 7). d_{SLG} is taken to be the vertical distance between the interfaces in the case of the wetting film, and d_{GLG} the horizontal distance in the case of the thin film between bubbles. The results for four such cycles (which together cover the whole range of *Ca*) are shown in Fig. 7. Focusing on the scaling regime (solid line) the results overlap perfectly, which demonstrates that the chosen disjoining pressures have no influence on the physical quantities here.

For a two-dimensional (2D) model, computational times and memory requirements are generally low. However, for small *Ca* values, the dimension of the wetting film are much smaller than those of the Plateau borders. This difference in length scales implies a very fine mesh which dramatically increases memory requirements. With our calculations we reached the limits of a 2 Gbytes RAM computer.

IV. RESULTS

A. General description

We have computed the bubble shapes and corresponding flow fields for a wide range of capillary numbers *Ca* and bubble lengths L_{per}. Key features of the results are schematically indicated in Fig. 8. The velocity field $\underline{u}(x,y)$ and the dynamic pressure field $p(x,y)$ are shown in Fig. 9 for three different values of *Ca* with $L_{\mathrm{per}}=4$.

The overall flow pattern consists of a slow-moving, anticlockwise vortex in the Plateau border region and a fast-moving, plug-like flow in the wetting film. As already emphasized by Bretherton,[10] the entrance and exit of the wetting film play a major role in the global behavior of the system. At the entrance to the narrow film (on the left-hand side), the convergence of the flow is associated with a significant increase in pressure. This reaches an approximately constant value equal to the gas pressure P_G so that the film thickness remains almost constant. At the other end of the wetting film

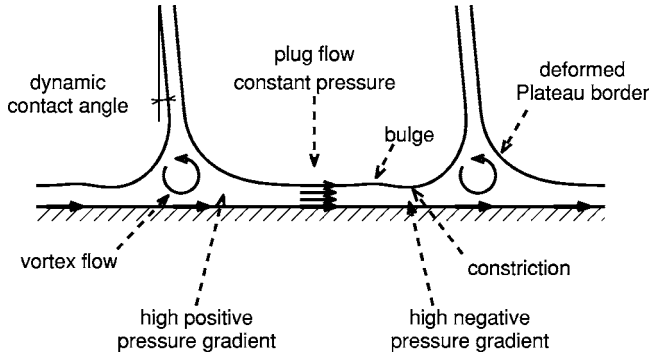

FIG. 8. Sketch of the key features of the bubble shape and flow field obtained in the simulations. We obtain plug-like flow in the wetting film and a slow-moving vortex in the Plateau border. The downstream end of the wetting film forms a constriction, which is preceded by a small bulge.

there is a divergent flow into the Plateau border and a corresponding reduction of pressure. This leads to the formation of a *constriction*, which has been theoretically predicted[6,10] and experimentally observed[6] by various researchers. For small capillary numbers, this constriction is preceded by a small bulge. Both features are most evident in Fig. 10, which shows the variation of curvature along the gas/liquid interface.

The thin films between the bubbles are canted at an angle, which is required for the external forces to be in balance.

B. Shape properties

With increasing capillary number *Ca* the bubble deforms notably and the thickness of the wetting film grows. This contributes significantly to an increase of the area A_L of the liquid domain Ω_L, as a consequence of the constant pressure condition applied in the film between the bubbles (Sec. II B).

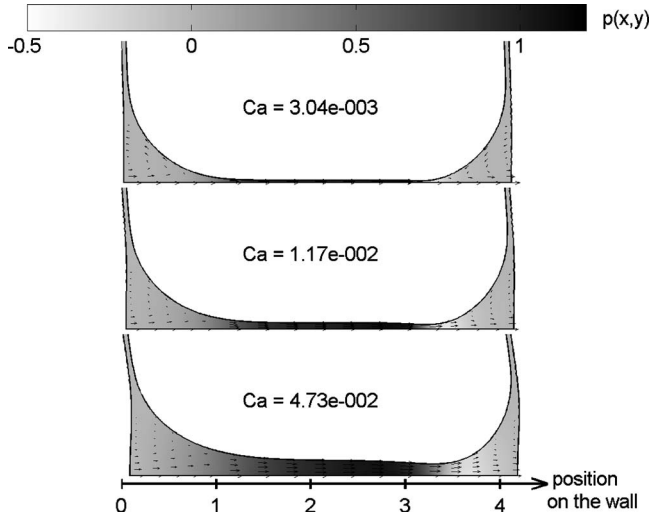

FIG. 9. Equilibrium bubble shapes, velocity profiles and dynamic pressure fields $(p(x,y)=p_L-P_L)$ for three different values of *Ca*. The bubble is increasingly sheared and the wetting film thickens significantly toward higher *Ca*.

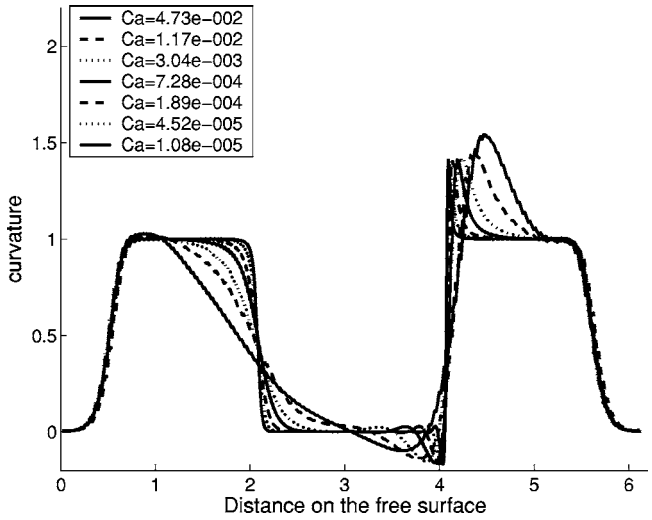

FIG. 10. Curvature along the free interface for different values of *Ca*. The distance on the free interface is measured from the upper left end of the gas/liquid interface.

Taking h_{film} as the thickness at the center of the wetting film, its variation with *Ca* is shown in Fig. 11. This conforms very well to a power law

$$h_{\text{film}} = 1.25\ Ca^{0.66} \tag{45}$$

over a large range of *Ca*.

Bretherton[10] obtained

$$h_{\text{film}} = 1.33\ Ca^{2/3} \tag{46}$$

for $Ca < 10^{-3}$, using the lubrication approximation. He also predicted for the height of the constriction

$$h_{\text{cons}} = 0.716\ h_{\text{film}}. \tag{47}$$

Fitting our simulations for $Ca < 10^{-3}$, we precisely confirm this relationship. Over the whole range of *Ca* we find (Fig. 11)

$$h_{\text{cons}} = 0.753\ h_{\text{film}}. \tag{48}$$

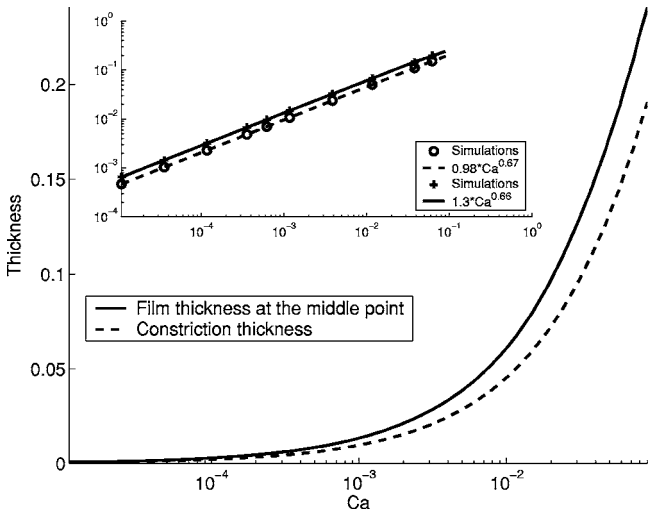

FIG. 11. Variation of the wetting film thickness in the middle of the film and at the constriction with *Ca*. Both conform very well to power laws [Eqs. (46) and (48)]; see the inserted log-log plot of the same data.

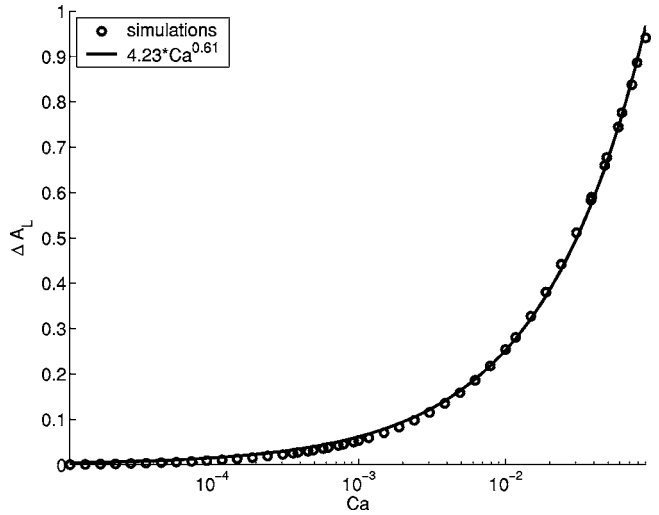

FIG. 12. Increase ΔA_L of the liquid area A_L with Ca. The results are fitted well by a power law [Eq. (49)], which can be attributed to the fact that most of the area increase is related to the thickening of the wetting film, and hence to Eq. (46).

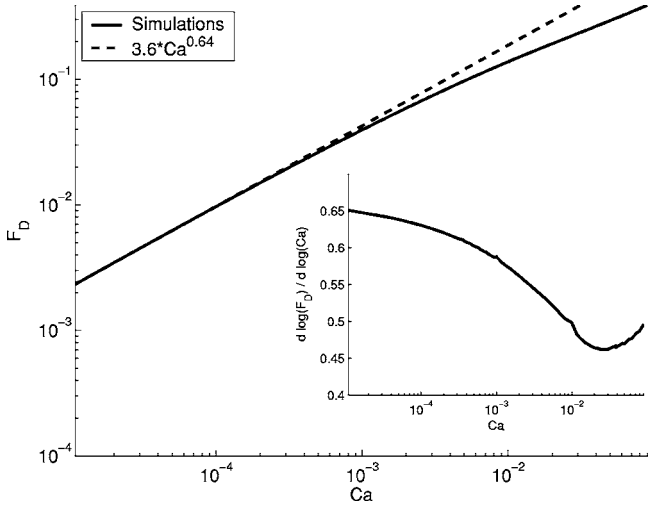

FIG. 14. Total dissipative force F_D [Eq. (31)] exerted on the wall as a function of Ca. The insert shows the slope, which corresponds to the power n in the relation $F \propto Ca^n$ [Eq. (1)] whenever it is reasonably constant. This is only the case for small Ca.

The increase of area ΔA_L [defined as the difference between the dynamic and static area $A_L - A_L(Ca=0)$] of the liquid domain with Ca is shown in Fig. 12. It is fitted by a power law

$$\Delta A_L = 4.23\ Ca^{0.61}. \tag{49}$$

This may be compared with the expectation based on Eq. (46), attributing the area increase to the change of film thickness. Recalling that the system is of length $L_{\mathrm{per}}=4$ there is rough agreement with this crude estimate.

C. Force on the wall

The tangential component of the viscous stress $(\underline{t} \cdot \underline{\underline{\sigma}} \cdot \underline{n})$ at the wall is shown in Fig. 13 for a range of Ca. It varies considerably with position.

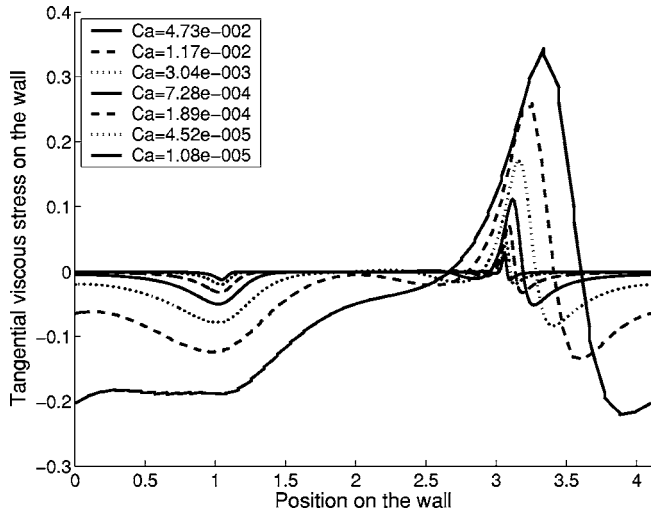

FIG. 13. Distribution of the tangential viscous stress $(\underline{t} \cdot \underline{\underline{\sigma}} \cdot \underline{n})$ along the wall of the periodic cell for various values of Ca (the same as in Fig. 9). The stress at the exit of the wetting film displays a pronounced peak of *opposite* sign.

The stress is negligibly small in the wetting film for small Ca, as a result of the plug-like nature of the flow. For larger Ca the thickness of the wetting film varies with position, leading to finite wall stress. However, this contribution remains negligible when compared to the stresses concentrated at the entrance and exit of the film. These two regions display significantly different features. On the right-hand side we observe large positive stress in the constriction, which is followed by a region of negative stress. For the left-hand part the stress is in the same direction (negative) everywhere.

The total dissipative force F_D exerted by the bubble on the wall is given by the integration of the tangential stress $\underline{t} \cdot \underline{\underline{\sigma}} \cdot \underline{n}$ along the wall according to Eq. (31). As Fig. 13 illustrates, this is almost entirely associated with the entry of the liquid into the wetting film; on the other side of the film contributions of the positive and negative stress before and after the constriction roughly cancel. This corroborates previous analyses.[6,9,10]

A log-log plot of the total force F_D vs Ca is shown in Fig. 14. The inset shows the value of

$$n = \frac{\partial \log(F_D)}{\partial \log(Ca)}, \tag{50}$$

which should be constant wherever F_D is related to Ca by a power law.

Unlike in the case of the wetting film thickness, no unique power law is satisfactory over the entire range of Ca. In the limit of small capillary numbers ($Ca < 10^{-3}$), the lubrication approximation power law with $n=2/3$ is recovered, as predicted by Bretherton[10] and confirmed by Ratulowski.[30] In this limit we obtain

$$F_D = 3.60\ Ca^{0.64}, \tag{51}$$

which compares very well to Bretherton's prediction of

$$F_D = 3.73\ Ca^{2/3}. \tag{52}$$

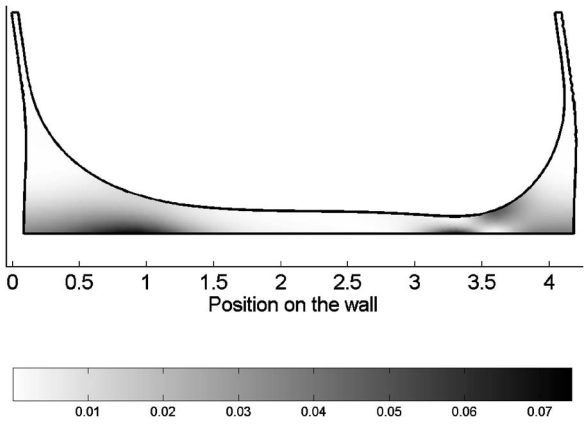

FIG. 15. Viscous dissipation field for $Ca=4.73\times10^{-2}$. It emphasizes the role of the entrance and the exit of the wetting film.

D. Viscous dissipation

An example of the distribution of the local viscous dissipation rate in the system is shown in Fig. 15 for $Ca=4.73\times10^{-2}$. Pronounced features of this distribution are again found near the entrance and exit region of the wetting film. In the entrance region (left), most dissipation occurs near the wall. In the exit region (right), part of the dissipation is localized on the wall before and after the constriction, while another part is concentrated on the gas/liquid interface just after the constriction.

The power required to push the bubble at the velocity specified by Ca is dissipated throughout the viscous liquid and therefore given as an integral of local contributions by

$$F_D \times Ca = \int_{\Omega_L} 2\eta_B \underline{\underline{\epsilon}} : \underline{\underline{\epsilon}} \tag{53}$$

in terms of the deformation rate tensor $\underline{\underline{\epsilon}}$ [Eq. (7)].

In order to visualize the variation of the dissipation rate along the x axis, we integrate $2\eta_B \underline{\underline{\epsilon}} : \underline{\underline{\epsilon}}$ along the y axis at each point. The result is normalized by the total dissipation rate and plotted in Fig. 16 for various values of Ca.

In contrast to the case of the tangential wall stress (Sec. IV C), the contribution of both ends of the wetting film is approximately equal. The graph also shows that the two regions of significant dissipation increase in width with Ca. Beyond $Ca\approx10^{-3}$ the two regions begin to interact through the Plateau border.

E. Influence of bubble size

We have described a flow pattern of plug flow and end effects. Our results remain essentially the same provided that the wetting film is long enough to permit this plug flow. In the Bretherton regime ($Ca<10^{-3}$), the end effects extend over regions which scale as $Ca^{1/3}$.[6,10] Thus there remains a region of plug flow provided that

$$\frac{L_{\text{film}}}{Ca^{1/3}} > \xi, \tag{54}$$

where the constant ξ is found to be approximately 10 in our simulations. To illustrate this, Fig. 17 shows that L_{per} ($L_{\text{film}}=L_{\text{per}}-2$) has negligible influence on the relationship between F_D and Ca. Only when the length of the wetting film becomes of the order of the Plateau border size ($L_{\text{film}}\approx2$) do we begin to see a small deviation in the slope of the curve for larger Ca. More insight into the disappearance of the flat-film region in the wetting film for high Ca can be gained in Figs. 10 and 14. The appearance of a finite wall stress at the center of the wetting film is in agreement with a small but nonzero dissipation all along the wetting film for $Ca=4.73\times10^{-2}$ and $L_{\text{per}}=4$.

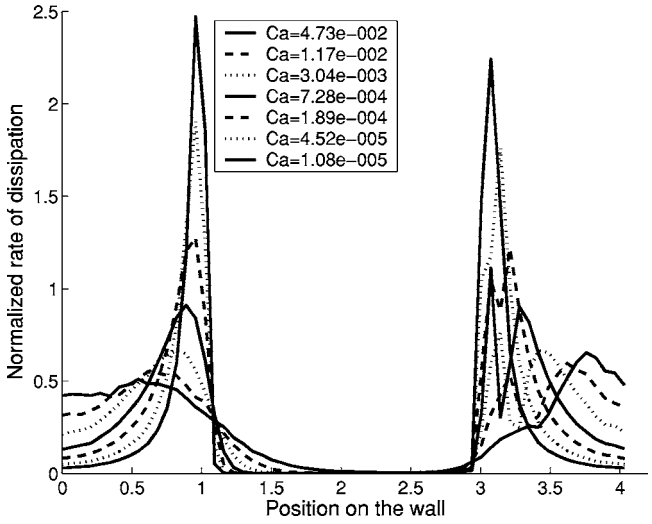

FIG. 16. Variation of the integrated and normalized viscous dissipation along the wall of the periodic cell for the same Ca as in Figs. 13 and 10. This emphasizes the dominance and similar magnitude of the dissipation at the entrance and exit of the wetting film.

V. FINITE INTERFACE MOBILITIES

All previous sections apply to mobile interfaces. In real systems, a finite surface viscosity or elastic effects oppose surface shear and the surface is not fully mobile. In some

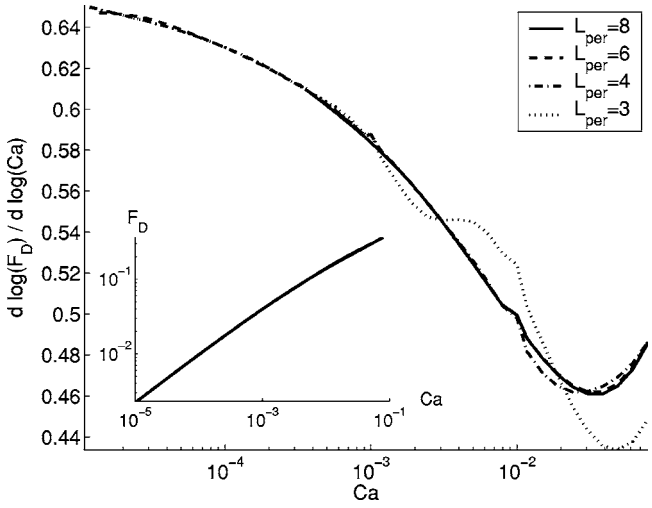

FIG. 17. Investigation of the influence of the bubble length L_{per} on the relationship between F_D and Ca. The film length is given by $L_{\text{film}}=L_{\text{per}}-2$. We see that it has little influence. For small values of $L_{\text{per}}<4$ small deviations begin to show up in the slope at high Ca.

cases the interface may be considered *immobile*. This limiting case was considered by Denkov *et al.*[6] However, neither these authors nor previous authors have confronted the effect of the inevitable surface stresses associated with finite surface mobilities upon the equilibrium shape of the interface. With this in mind we have hesitated to explore this case of an immobile surface, since we are uncertain as to how such effects may be incorporated in a 2D model.

We did perform some calculations in the spirit of Denkov *et al.*,[6] ignoring this problem, and obtained results reasonably consistent with these authors. In particular, the viscous force scales as

$$F_D \propto Ca^{0.440}, \tag{55}$$

compared with

$$F_D \propto Ca^{0.5}. \tag{56}$$

(Ref. 6).

VI. CONCLUSION

Our results confirm the theoretical scaling results within the appropriate regime in which the previous approximations hold. Roughly speaking, this regime is confined to approximately $Ca < 10^{-3}$ and $L_{\mathrm{film}} > 10\ Ca^{1/3}$, as explained in Secs. IV C and IV E. Beyond this regime, our simulations give some indication of the departures from scaling which are to be expected in experiments.

Other insights have been gained from scrutiny of the detailed flow pattern. Note in particular that the dissipation is concentrated at both ends of the system, in roughly equal amounts (Sec. IV D). There is no necessary relation between this distribution and that of the tangential viscous stress on the wall (Sec. IV C), other than the balance of the total rate of dissipation and the power input at the wall.

The variation of the liquid area (corresponding to volume if the system is extended in the third dimension) with *Ca* may have relevance to *dilatancy* in foams. This is an increase of the amount of liquid in a foam with strain and/or strain rate, which has been introduced by Weaire and Hutzler.[31] This effect is more familiar in the mechanics of granular materials but may play a significant role in foams also. In particular it has been invoked as a possible factor in the explanation of convective instability.[32] The result shown in Fig. 12 pertains to what we might call *surface dynamic dilatancy*.

Most foam flow problems are well described by the scenario presented here, namely one in which the difference in pressures between adjacent bubbles is much less than the difference in pressure between the bubbles and the liquid. This assumption may break down in recent developments in microfluidics, which deal with highly dissipative foam flow in narrow channels.[3,13] Future simulations will have to investigate how the additional pressure gradient influences the bubble shape and also the resulting *pressure driven drainage*[2] between adjacent Plateau borders. Such studies may also consider a constant volume constraint in place of the constant pressure condition (Sec. II B).

More generally, there remain many other problems in foam physics in which this kind of self-consistent simulation of flow pattern and surface equilibrium would be illuminating. The success of the present exercise gives some hope of rapid progress on the three-dimensional problems which link local behavior to continuum theories of drainage and rheology.

An important example is that of the flow through the node or junction at the confluence of a number of Plateau borders (usually four) in a bulk foam. The properties of this junction are significant in the theory of foam drainage. The effect of its deformation and possible instability at high flow rates has not been analyzed.

ACKNOWLEDGMENTS

The authors would like to thank N. Denkov and I. Cantat for stimulating discussions at the FRIT workshop (http://users.aber.ac.uk/sxc/frit.html) organized by S. J. Cox. The research was funded by the European Space Agency (MAP AO-99-108:C14914/02/NL/SH, MAP AO-99-075:C14308/00/NL/SH), Enterprise Ireland (BRG SC/2002/011), and the Science Foundation Ireland (RFP 05/RFP/PHY0016). One of the authors (A.S.) was supported by the Conseil Régional de Rhône-Alpes. Another author (W.D.) is an IRCSET Fellow funded by the Embark Initiative Ireland.

[1] D. Exerova and P. M. Kruglyakov, *Foam and Foam Films; Theory, Experiment, Application* (Elsevier Science, Amsterdam, The Netherlands, 1998).
[2] D. Weaire and S. Hutzler, *The Physics of Foams* (Clarendon, Oxford, 1999).
[3] W. Drenckhan, S. J. Cox, G. Delaney, H. Holste, D. Weaire, and N. Kern, "Rheology of ordered foams. on the way to discrete microfluidics," Colloids Surf., A **263**, 52 (2005).
[4] R. Höhler and S. Cohen-Addad, "Rheology of liquid foam," J. Phys. Condens. Matter **17**, R1041 (2005), and references therein.
[5] E. Janiaud and F. Graner, "Foam in a two-dimensional couette shear: A local measurement of bubble deformation," J. Fluid Mech. **532**, 243 (2005).
[6] N. D. Denkov, V. Subramanian, D. Gurovich, and A. Lips, "Wall slip and viscous dissipation in sheared foams: Effect of surface mobility," Colloids Surf., A **263**, 129 (2005).
[7] D. Weaire, S. Hutzler, and N. Pittet. "Cylindrical packings of foam cells," Forma **7**, 259 (1992).
[8] N. Pittet, N. Rivier, and D. Weaire, "Cylindrical packing of foam cells," Forma **10**, 65 (1995).
[9] I. Cantat, R. Delannay, and N. Kern, "Dissipation in foam flowing through narrow channels," Europhys. Lett. **65**, 726 (2004).
[10] F. P. Bretherton, "The motion of long bubbles in tubes," J. Fluid Mech. **10**, 166 (1961).
[11] A. M. Kraynik, "Foam flows," Annu. Rev. Fluid Mech. **20**, 325 (1988).
[12] H. M. Princen, "Rheology of foams and highly concentrated emulsions. 2. Experimental-study of the yield stress and wall effects for concentrated oil-in-water emulsions," J. Colloid Interface Sci. **105**, 150 (1985).
[13] E. Terriac, J. Etrillard, and I. Cantat, "Viscous force exerted on a foam at a solid boundary: influence of the liquid fraction and of the bubble size," Europhys. Lett. (in press).
[14] N. Kern, D. Weaire, A. Martin, S. Hutzler, and S. J. Cox, "The two-dimensional viscous froth model for foam dynamics," Phys. Rev. E **70**, 041411 (2004).
[15] S. Cox, G. Bradley, S. Hutzler, and D. Weaire, "Vertex correction in the theory of foam drainage," J. Phys.: Condens. Matter **13**, 4863 (2001).
[16] S. A. Koehler, S. Hilgenfeldt, and H. A. Stone, "Foam drainage on the microscale i. modeling flow through single plateau borders," J. Colloid Interface Sci. **276**, 420 (2004).
[17] A. V. Nguyen, "Liquid drainage in single plateau borders in foams," J. Colloid Interface Sci. **249**, 194 (2002).

[18]C. Marangoni, "Über die Ausbreitung der Tropfen einer Flüssigkeit auf der Oberflöche einer anderen," Ann. Phys. **143**, 337 (1871).
[19]M. Durand and D. Langevin, "Physicochemical approach to the theory of foam drainage," Eur. Phys. J. E **7**, 35 (2002).
[20]J. Israelachvili, *Intermolecular and Surface Forces* (Academic, London, 1995).
[21]J. L. Barrat and J. P. Hansen, *Basic Concepts for Simple and Complex Fluids* (Cambridge University Press, Cambridge, MA, 1983).
[22]D. A. Edwards, H. Brenner, and D. T. Wasan, *Interfacial Transport Processes and Rheology*, Butterworth-Heinemann Series in Chemical Engineering (Butterworth-Heinemann, London, 1991).
[23]P. A. Sackinger, P. R. Schunk, and R. R. Rao, "A Newton-Raphson pseudo-solid domain mapping technique for free and moving boundary problems: a finite element implementation," J. Comput. Phys. **125**, 83 (1996).
[24]R. A. Cairncross, P. R. Schunk, T. A. Baer, P. A. Sackinger, and R. R. Rao, "A finite element method for free surface flows of incompressible fluids in three dimensions I. Boundary fitted mesh motion," Int. J. Numer. Methods Fluids **33**, 375 (2000).
[25]T. A. Baer, R. A. Cairncross, P. R. Schunk, R. R. Rao, and P. A. Sackinger, "A finite element method for free surface flows of incompressible fluids in three dimensions II. Dynamic wetting lines," Int. J. Numer. Methods Fluids **33**, 405 (2000).
[26]H. Braess and P. Wriggers, "Arbitrary Lagrangian Eulerian finite element analysis of free surface flow," Comput. Methods Appl. Mech. Eng. **190**, 95 (2000).
[27]M. A. Walkley, P. H. Gaskell, P. K. Jimack, M. A. Kelmanson, and J. L. Summers, "Finite element simulation of three dimensional free surface flow problems," Int. J. Numer. Methods Fluids **47**, 1353 (2005).
[28]R. L. Taylor and O. C. Zienkiewicz, *The Finite Element Method* (Butterworth-Heinemann, Oxford, 2000), Vols. 1–3.
[29]J. Salencon, *Handbook of Continuum Mechanics: General Concepts, Thermoelasticity* (Springer, Berlin, 2001).
[30]J. Ratulowski and H.-C. Chang, "Transport of gas bubbles in capillaries," Phys. Fluids A **1**, 1642 (1989).
[31]D. Weaire and S. Hutzler, "Dilatancy in liquid foams," Philos. Mag. **83**, 2747 (2003).
[32]S. Hutzler, D. Weaire, and R. Crawford, "Convective instability in foam drainage," Europhys. Lett. **41**, 461 (1998).